In situ interfacial nanoengineering of imidazole-bridged one-dimensional AgVO₃ nanoribbons by Ag fractals

Sarigamala, K.K.; Albrecht, T.; Shukla, S.; Saxena, S.

[Link to publication on Research at Birmingham portal](#)

In-Situ Interfacial Nanoengineering of Imidazole Bridged-1D AgVO₃ Nanoribbons by Ag fractals

Karthik Kiran Sarigamala[1], Tim Albrecht[2], Shobha Shukla[3], and Sumit Saxena[3]

[1]Centre for Research in Nanotechnology and Science, Indian Institute of Technology Bombay, Mumbai, MH, India - 400076.
[2]School of Chemistry, University of Birmingham, Edgbaston, Birmingham, United Kingdom, B15 2TT.
[3]Nanostructures Engineering and Modelling Laboratory, Department of Metallurgical Engineering and Materials Science, Indian Institute of Technology Bombay, Mumbai, MH, India - 400076.

Abstract

The major bottleneck in harnessing the potential of solid-solid interfacial heterostructures involves incoherent interface constructions and complicated synthesis approaches. In this context, a synthesis strategy involving in-situ interfacial manipulation of imidazole bridge done dimensional (1D) single-crystalline nanoribbons is developed through dynamic growth of Ag fractals. This manuscript successfully demonstrates structural and morphological changes on the monoclinic patterns of silver vanadate nanoribbons with Wulf constructions. These are associated with in-situ electron beam perturbations and attributed to β-phase silver vanadate crystals. The dynamics and topological modifications induced on the nanohybrid interfaces mechanistically suggests the ability of the novel hybrid interfaces in harnessing and storing photogenerated auxiliary charge carriers. The synthesis methodology used enables in overcoming major bottleneck in nanoengineering of solid-solid interfacial heterostructures by utilizing real-time feedback of the imaging e-beam to precisely fabricate these heterostructures and study the interface transition.

Introduction

Synthesizing exotic 1D hybrid interfaces with noble metal nanoparticles as surface-active sites is an attractive concept, but challenging (1-3). Blending metallic silver nanoparticles in vanadium oxide nano frameworks as an ultimate material has attracted considerable attention promising a broad spectrum of synergistic and integral characteristics. These are anticipated to find potential applications in energy storage, catalyst supports for surface-enhanced Raman spectroscopy, sensors, and biomedical devices, to name a few (4-8).Synthesis of such hybrid interfaces is however is an ardent task for which no traditional solution exists (9).Various synthesis approaches have been explored to synthesize such hybrid interfaces on Ag_2WO_4, Ag_3PO_4 and Ag_2CrO_4 and β-$AgVO_3$(10-15), unfortunately lacks dynamic and tight control of fractal interfaces. Thus, exploration of unconventional synthesis method needs to be explored. Electron beam-based methods provide tight control of atomic arrangement. The e-beam mediated synthesis of interfacial morphologies plays a crucial role in tuning the characteristics of the core surfaces. Using electron beam source in imaging devices such as scanning and tunnelling electron microscopes provide real time dynamic control in nanofabrication of heterostructures. In this perspective a simple approach of using imaging electron beam, available in electron microscopes, to drive materials chemistry at nanoscale is rapidly growing.

Here we have synthesized 1D β-$AgVO_3$nanoribbons by imidazole complexation as solid precursors to tailor surface engineering process, using imaging e-beam under high vacuum. The specimen is restructured into a hetero-structure fractal interface through in-situ nucleation and monitoring the growth of silver nanostructures when exposed to e-beam irradiation. The dynamic process involves generation of localized serrations, which are governed by the rate of the generated and annihilated defects/dislocations. Probing the dynamics and topography of the surface and interfaces revealed that the growth of metallic

57 Ag nanoparticles on semiconducting interfaces results in the cleavage of the electron-hole

58 pair with increasing separation and the SPR effect would amplify the light absorption

59 capacity (17). The charge transfer interactions induced due to SPR effect uncovers the

60 immense potential of the heterostructure in electrochemical energy storage applications as

61 well. This synthesis methodology enabled in nanoengineering of solid-solid interfacial

62 heterostructures of Ag/AgVO$_3$ interface along with real-time feedback of the imaging e-beam

63 to precisely fabricate these heterostructures and study the interface transition.

64 **Results and discussion**

65 The synthesis mechanism is shown in Figure 1(a). Imidazole, when dissolved in the solvent,

66 its unprotonated molecule acts as ligand through the unshared pair of electrons on pyridinic

67 nitrogen. The pyridinic nitrogen acts as a ligand site due to large electronegativity. Hence,

68 complex formation is conceivable by ligation with metallic ions (18). Subsequently, the metal

69 (silver) imidazolate complex formation occurs during the oxidation process. Conversely, a

70 silver cation co-ordinate with one more nitrogen ligand. During the chemical reaction, the

71 imidazole anions act as bridging ligands to co-ordinate with silver cations resulting in

72 formation of complex bridging chain (19). When sufficient energy is supplied, the chain

73 breaks and growth of heterostructure is initiated.

74 The elemental maps in Figure 1(b) shows the homogeneous distribution of Ag, V, and

75 O over the surface of the nanoribbon before the growth. The selected area diffraction (SAED)

76 pattern obtained from the nanoribbon shown in Figure 1(c) was indexed to the crystal lattice

77 planes of β-AgVO$_3$(Supporting information, Figure S1). The SAED spots reveal single-

78 crystalline nature of the nanoribbons with diffraction planes assigned to (110), (-111), (111)

79 and (710) of β-AgVO$_3$.
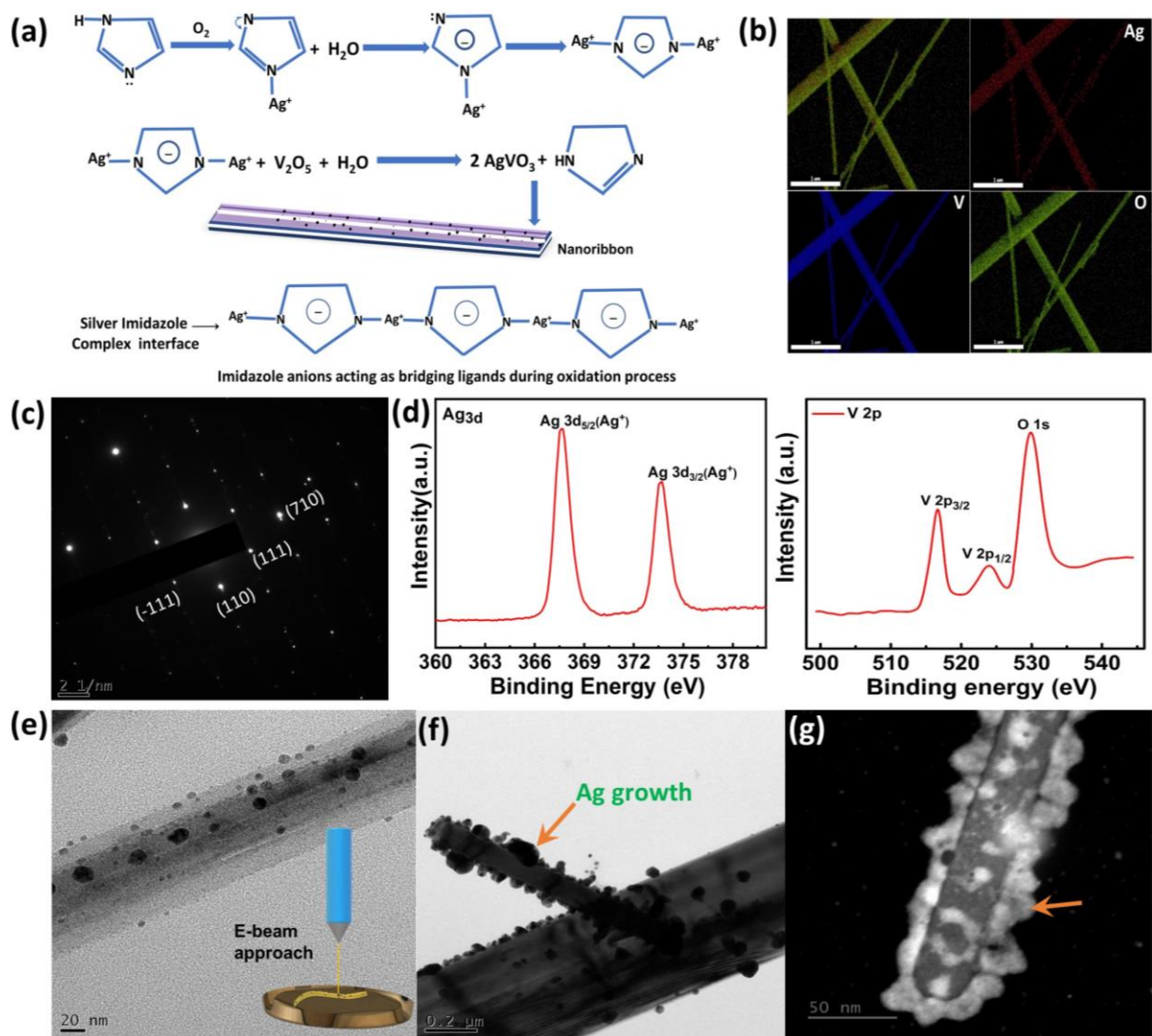
Figure 1. *(a) Schematic showing reaction mechanism and the growth of β-AgVO₃ ribbons.(b) EnergydispersiveX-ray spectroscopy(EDS)elemental maps of the β-AgVO₃ ribbons. (c) SAED pattern of β-AgVO₃ nanoribbon indexed to corresponding lattice planes. (d)XPS spectra of β-AgVO₃ with high resolution peaks obtained for Ag 3d, V 2p and O 1s spectra respectively.(e) TEM micrograph showing the effect of electron beam interaction with the nanoribbon and in-situ grown Ag nanoparticles, (f)&(g) TEM and STEM micrographs showing the growth of nanofractals respectively.*

To understanding the chemical structure, purity, and valance states of the β-AgVO₃ ribbons

X-ray photoelectron spectroscopy (XPS) spectra was obtained and shown in Figure 1(d).

High-resolution XPS spectra obtained for the elements Ag, V and O have binding energies

corrected for charge offset by referencing C1s peak from surface adsorbed carbon at 284.8

eV. The hyperfine splitting of V2p core levels results in the photoemission at 516.6 eV and

93   524.2 eV. Single core level emission at529.8 eV corresponding to O1s is observed. The

94   high-resolution spectra of Ag 3d shows two firm Ag^+ peaks at 367.3 eV and 373.5 eV

95   corresponding to Ag $3d_{(5/2)}$ and Ag $3d_{(3/2)}$.The restructuring and growth phenomenon under

96   the influence of an electron beam over a 1D $AgVO_3$ nanostructure support specimen is

97   demonstrated in the study. Surface restructured process over crystalline nanoribbon is shown

98   in Figure 1(e)-inset (A schematic illustration of e-beam process is shown; and for reference

99   the morphology of pristine nanoribbons without Agis shown in supporting Figure S2). The

100   solid support specimen has multiple spots of contact with the conductive grid which assists in

101   eliminating both thermal spikes and charging effects. The beam restructures the nanoribbon

102   by channelling electronic energy to the targeted location. At sufficient energy, the beam

103   ionizes the inner shell (20).

104   The energetic distribution of electrons over the bulk/surface induces electron-solid

105   interactions (21). The electron trap-mediated reduction route drives the initial segregation of

106   Ag nanoparticles. The TEM allows for examining the electron beam's role in Ag segregation

107   trails by initial stages of nucleation followed by the growth of fractals. Exposure to a

108   relatively low intense incident electron beam with a dose rate of 2.0-20.0 e $Å^{-2}$ s^{-1} allows us

109   to create a small cluster of Ag nanoparticles (2-5nm), as shown in Fig 1(e). From such

110   considerations, as a function of electron beam illumination parameters, we can predict that

111   through electron trapping, especially at the local defect sites, reduction of the Ag^+ to Ag^0 is

112   initiated. During this early stage of the electron bombardment process, the beam stimulates

113   charging effects with incongruent dissipation of thermal energy over the core to create local

114   defects. These defects create hot spots for the accumulation of electrons inducing Coulombic

115   forces (22). The electrostatic field then mobilises the ionised Ag nanoparticles, which were

116   fragmented from the bonded Ag clusters. More incident electrons passing through interaction

117   volume for a more considerable dwell time result in added ionization scattering events per

118   scan (For additional information, see Fig. S6), which would be adequate for surplus growth

119   of Ag particles with diameters of about 10 nm (See Fig S5 (b), (d) and (f)) (23,

120   24).Subsequently, as a function of time with an increase in cumulative electron dose (electron

121   dose rates in the range of ~60-100e $Å^{-2}$ s^{-1}), the onset of coalescing Ag nanoparticles

122   transcends at the nucleation edges. Random progression of Ag coalesces and diffusion-driven

123   phenomenon under high beam currents resulted in Ag fractal growth (50-100nm) with

124   structural transitions, as shown in Fig 1(f).   The temperature gradient further drives

125   nucleation outwards the nanoribbon surface. Hence the growth of the Ag fractals is preferably

126   oriented along the edges of the support in lateral dimensions.

127   In scanning transmission electron microscopic (STEM) mode, a high angle annular dark-field

128   (HAADF) image was acquired to ensure that only electrons deflected by larger angles were

129   collected. Here we elucidated the effects on the sample support using the standard STEM

130   approach of scanning the image sequentially. The STEM probe is held on each pixel in the

131   micrograph, defining how fast the electron beam is rastered across the sample. Generally,

132   STEM imaging will cause more severe electron induction than regular TEM mode operation

133   damaging the specimen, and large beam currents may also induce sublimation effects (25).

134   For comparison, HAADF- STEM imaging was also carried out in cryo-mode and assessed

135   with HAADF-STEM images under ambient temperature conditions, as shown in supporting

136   Fig. S9. The micrograph shown in Fig. S9 (b) has an apparent beam damage effect on the

137   sample surface during prolonged exposure to the sample during STEM image data acquisition

138   under ambient conditions. STEM data collected in cryo-mode (Fig. S9 (c)) using

139   cryogenically cooled specimen offered low electron induction, which mitigated thermal

140   decompositions to reduce the Joule heating effect and thermal diffusion (Details of the

141   cryogenic cooling experiment is provided under the methods section and represented using a

142   schematic in supporting information of Fig. S9. As shown in Fig S9 (d), a corresponding

143 EELS spectrum was also obtained. Thus, when STEM beam parameters are accommodated

144 below a critical threshold, it will help us understand the growth dynamics under ambient

145 temperature conditions. Hence fast scanning approach or changing the pixel dwell time

146 during image acquisition is applied for low electron fluence. The incident electron beam was

147 used as the STEM imaging probe and the ionising radiation source to stimulate growth by

148 electron beam reduction. The actual exposure also relies on the time devoured in

149 accumulating the data. Hence room temperature STEM mode image was obtained from a

150 specific area within a controlled time, allowing us to evaluate the structural transition as a

151 function of the total electron dose. From Fig 1(g), the scatter to high angles in the base region

152 of the nanoribbon support decreased due to increased lattice disorder, and these regions have

153 reduced intensity which displays reduction. Thus, under higher dose rates, the contrast

154 variation spread is noticed from the base to the support edges. An additional contrast

155 transition was observed at the periphery, associated with vacancy ordering and forming Ag

156 fractals. From these observations, it appears that the beam current is analogous to the

157 concentration of reducing agents for the growth of nanoparticles. Accordingly, the in-situ

158 electron beam ionization of nanoribbon surface suggests that diffusion assisted process

159 favours the growth of Ag fractals. Consequently, the transformation of Ag fractals to

160 dendritic structures along the surface manifests the predominance of anisotropy over random

161 progression of Ag aggregates. Thus, the segregation of the Ag nanoparticles provides high

162 local charge densities and alter the surface potential (26). For a clear conception of the lattice

163 defects that bend over the lattice planes, the incident beam is tilted just off Bragg's condition

164 providing high resolution, mass-dependent low noise images. The surrounding matrix with

165 densely accumulated charges renders the nanoparticles to interface with the nanoribbon

166 support. The interfacial confinement of these metal nanostructures on the surface of the

167 semiconducting nanoribbons

168
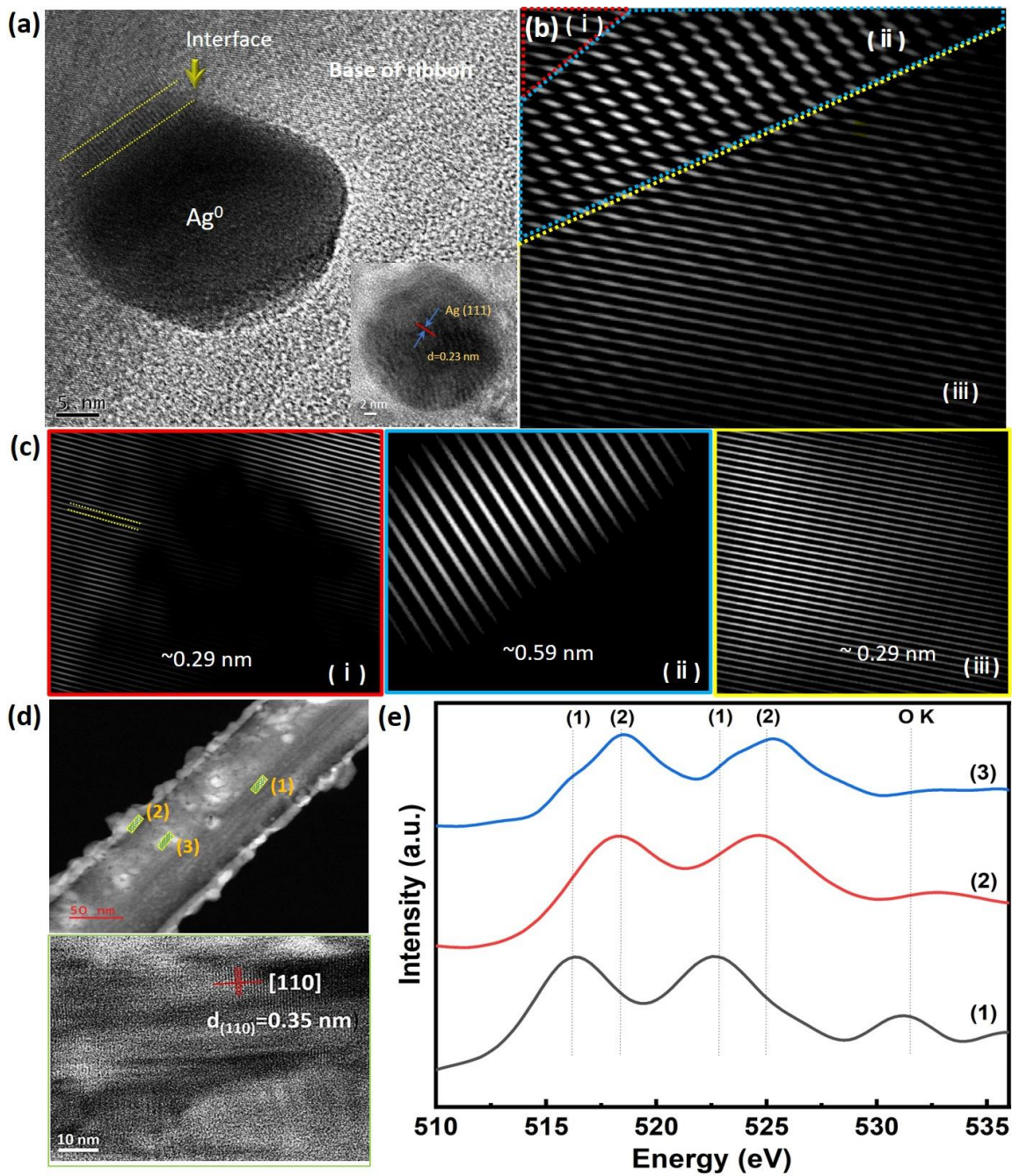
Figure 2. *(a) Ag/AgVO₃ interface (b) interplanar spacings of segmented section of interface, (c) IFFT images showing interplanar spacings with the section (i), (ii) and (iii), (d) EELS micrograph (HAADF image) acquired at three different locations of nanoribbon with inset (bottom) showing interplanar spacing of the nanoribbon and (e) EELS spectra showing contributions of V L and OK obtained at the desired regions.*

helps to passivate the surface defects and achieve better interfacial properties. The

phenomenon is anticipated to be supported by electron charge redistribution in the

177 nanoribbons due to electronic excitations coupled with the generation of silver vacancies

178 (27). The excess electrons during the direct electron-beam irradiation can stimulate electronic

179 and structural modifications in β-AgVO$_3$ crystals. The structural stability disturbed by

180 interaction of electrons results in the phase transformation and in the formation of oxygen (O)

181 and Ag vacancies. The following equation describes the growth process of Ag:

182 $$\beta\text{-AgVO}_3 + e^- \rightarrow Ag_{1-x}VO_3 + Ag^0$$

183 The nanoribbon's surface dynamics helps us to examine the transition state at high spatial

184 resolution using TEM. The Ag fractal dendrites in Figure 1 shows that the nucleation occurs

185 at the interface. Therefore, the transition at the interface area can be interjected with the

186 addition of interfacial states. Hence, a deeper understanding of the interface enables us to

187 explore the dynamics involved during the transition. The lattice fringes of the Ag/AgVO$_3$

188 heterostructure interface are obtained using high resolution transmission electron microscope

189 micrograph, as shown in Figure 2(a). The average diameter of Ag nanoparticle (inset) ranges

190 from 5-10 nm with a lattice spacing 0.23 nm, corresponds to (111) plane. The nucleated edge

191 and the growing edge can be seen alongside interface, and the crystal orientations are

192 different at the interfaces. The corresponding inverse fast Fourier transform (IFFT) image

193 was generated from high resolution interface and shown in Figure 2(b). Three diffraction

194 points are masked to simulate the IFFT along the interface. The lattice fringes at the edge

195 sections-1 & 3 and in the middle segment-2 of the interface show different inter-planar

196 spacing (Figure 2(c)). The phenomenon shows increase in crystal plane spacing in the

197 segment -2. The interplanar spacing of 0.59 nm is observed in segment -2, about two times as

198 long as segments 1 & 3 (~0.29 nm, corresponds to (-601) plane). The crystal plane

199 corresponding to the lattice spacing of 0.59 nm is not observed in the diffraction pattern from

200 XRD. This may be due to the introduction of new localized defect states resulting from

201 thermal fluctuations of the e-beam. The increase in the lattice spacing suggests phase

202 transformation during the growth of Ag crystallite on 1D $AgVO_3$ surface, confirming the

203 restructuring process in the nanoribbons. The electron beam may also create extended defects

204 besides point defects that act as trapping sites for the charge carriers and contribute to band

205 bending near the surface of the nanoribbons. This phenomenon reduces the bandgap and can

206 be verified using the UV-Vis and tauc-plots (supporting Figure S3). The UV-Vis spectrum of

207 irradiated $AgVO_3$nanoribbons show a broad absorption spectrum ranging from ultraviolet to

208 visible. An optical absorption band edge of ~1.59 eV is observed in the absorption spectrum

209 in contrast to ~2.01 eV reported for pristine $AgVO_3$(16). During the in-situ process, the

210 hybridization of Ag 5s orbital with Ag nanoparticles occurs, and the bandgap shifts below the

211 conduction band. Consequently, the bandgap is narrowed, resulting in Ag nanoparticles

212 conceivably increasing the rate of charge carriers at the interfaces. The broad visible

213 absorbance can be attributed to the SPR effect of bonded Ag^0 nanoparticles on the surfaces of

214 $AgVO_3$ nanoribbons. A representative high-resolution image showing additional interfacial

215 states is shown in the supporting Figure S4(b). This induced structural modification of

216 $AgVO_3$ nanoribbons with extrinsically bounded metal Ag nanostructures enhances the

217 interfacial charge transfer mechanism by improving the electron-hole separation (28). To

218 better understand this, electron energy loss spectroscopy (EELS) is performed. Top panel in

219 Figure 2(d) shows HAADF image shows the point of interest for obtaining the EELS spectra

220 (Figure 2(e)), bottom panel shows the HR-TEM image with interplanar spacing on the

221 nanoribbon surface. The EELS spectra corroborate the behaviour observed by HAADF-

222 STEM images. The potential influence on the specimen surface was analysed by conducting

223 corresponding EELS experiments. Changes in local chemistry or chemical bonding are

224 identified by tracking the fine structure of EELS spectroscopic data associated with the local

225 electronic structure. The EELS spectra obtained from the site with no Ag^0 nanoparticle

226 formation is marked as 1. Site-1 show two firm peaks at 516.3 eV and 522.7 eV, which

227 matches with Vanadium L3 and L2 edges, obtained from loss spectra during the excitation of

228 V 2p core states to unoccupied 3d states (L3, transition from 2p3/2 → 3d) and L2, transition

229 from 2p1/2 → 3d)), due to spin-orbit splitting. However, at the interface of the Ag fractals,

230 the V L3 and VL2 edges are shifted to higher energies of 518.2 eV and 524.04 eV,

231 respectively. This shift at the interface can be accounted to the atomic rearrangement with

232 silver vacancy diffusion and oxide formation in the Ag fractals with the migrated oxygen

233 species bonded to the silver nanoparticles. Further, the surface of the β-AgVO$_3$ with Ag

234 nanoparticles (region 3) has peak shifts at 518.5 eV and 525.1 eV. This suggests the presence

235 of vanadium in multiple oxidation states. An additional intense peak showing oxygen (O K)

236 appears from the base region with scarcely contained Ag^0 which shows numerous oxygen

237 defect sites in comparison to region at the interfacial surface of silver nanoparticles.

238 Scanning electron micrographs in Figure 3(a) & (b)) were used to study the topographical

239 surface features on the e-beam irradiated nanoribbons. The SEM micrograph shows small

240 silver nanoparticle clusters resembling nano shell formulations over the core surface serving

241 as "bridges". These provides path for the matter to move from one site to another during the

242 e-beam irradiation. Using FEG-SEM, the morphologies of AgVO$_3$ crystals were examined

243 with an operating range of 5–15 kV. The electron dose rate was varied at 100-250 e/A^{2}s for

244 the formation and nucleation of Ag NPs on the nanoribbons by adjusting the probe current

245 and the size of imaging area. Detailed visualization of the diffusion process under cumulative

246 electron dose in TEM was carried out at various time intervals and recorded (Supporting

247 Figure S6). The diffusion process further assisted the formation of the Ag lattices from the

248 initially merged Ag particle surfaces due to the thermal spikes induced on the metal surface

249 by bombarding high energy electrons (Figure 3(b) left panel t=0, right panel t=~150 s). Thus,

250 electron beam-assisted segregation of tiny Ag nanoparticles and growth of nanocrystals to
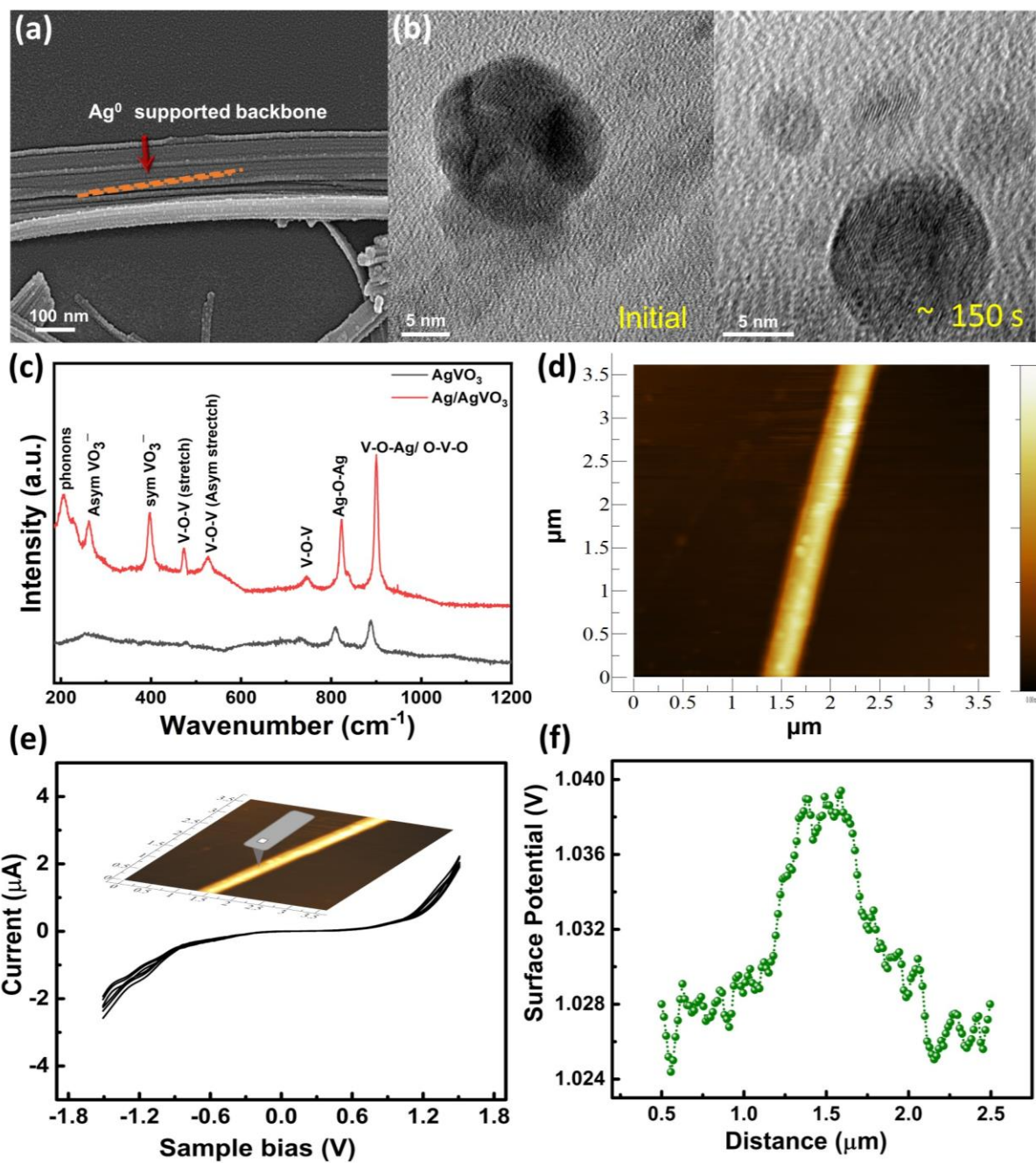
Figure 3. (a) & (b)FE-SEM and TEM micrographs showing the ionization effect on in-situ irradiated AgVO₃ nanoribbon respectively. (c) Raman spectra of the as prepared β-AgVO₃and e-beam irradiated sample (Ag/β-AgVO₃), (d) AFM image of the nanoribbon on which the conductive measurements are carried out, (e) I-V characteristics of the nanoribbon and(f) surface potential distribution of the ribbon.

fractal dendrites is thus closely analogous to conventional chemical reduction of nanocrystals, except for the presence of manifold reducing agents or oxidative species. The local defects on

the support specimen act as electron trap sites and intensify the reduction of the $AgVO_3$

support. The Raman spectra is obtained to determine the vibrational modes of the sample before

and after the e-beam irradiation on the sample as shown in Figure 3(c). The strong band at 887

cm^{-1} may originate from either-O-Ag or O-V-O vibrations. The band at 810 cm^{-1} is assigned

to vibrations of the Ag-O-Ag bridges. The bridging V-O-V bond chains is characterized by

the 732, 523 and 480 cm^{-1} stretching vibrations. The symmetric and asymmetric molecular

signatures of VO_3^- are observed at 396 cm^{-1} and 344 cm^{-1} respectively, while the symmetric

folding of VO_4^{3-} appears at 250 cm^{-1} representing channelled structure of $AgVO_3$. The

generated Ag nanoparticles result in surface plasmon resonance effect, which is observed

from Raman spectroscopy (Figure 3(c)). The e-beam irradiated sample displayed higher peak

intensities than pristine $AgVO_3$ nanoribbon due as a consequence of surface-enhanced Raman

scattering induced by Ag nanoparticles. Figure 3(d) shows the AFM micrograph on which the

conductive measurements were performed. Current-voltage (I–V) curves for a Ti/Ir coated tip

in contact with the nanoribbon is shown in Figure 3(e). All the obtained curves are nonlinear

and symmetric about the axis. The slope of the curve appears linear at low bias voltage of

0.8V. This region is used to evaluate the resistance of the nanoribbon and was found in the

range of 1.03×10^6 Ω - 1.42×10^6 Ω. At higher bias, above 1.5V the nonlinearity of curve

increases with sudden ramp in tip current resulting in degradation of the nanoribbon at the

point of contact with AFM tip. Kelvin probe force microscopy was used (29,30) to probe the

surface potential distribution and determine the work function. The surface potential

distribution over the width of the β-$AgVO_3$ nanoribbons in Figure 3(f) shows uniform surface

potential and charge distribution over the base while the potential distribution decreases

towards the edges of the nanoribbons with a work function of 3.88 eV. An increased

proportion of active electrochemical sites on the surface also effectively decrease the

polarization resistance and shorten the diffusion length.

Conclusion

In summary, multifunctional heterostructures were fabricated using an in-situ surface modification process of 1D β-AgVO$_3$ by the dynamic growth of Ag nanoclusters using an imaging e-beam. The nanoribbons with well-organized electron transport chain and many electroactive species were assembled by modulating the structural and chemical bonding/interactions. These are associated with in-situ electron beam perturbations and attributed to β-phase silver vanadate crystals. The dynamics and topological modifications induced on the nanohybrid interfaces mechanistically suggests the possibility of using novel hybrid interfaces in harnessing and storing photo generated auxiliary charge carriers. The synthesis methodology used enables in overcoming major bottleneck in nanoengineering of solid-solid interfacial heterostructures by providing real-time feedback to precisely fabricate these heterostructures and study the interface's transition.

Methods

Synthesis of solid precursor nanoribbons-

β-AgVO$_3$nanoribbons were prepared using hydrothermal reaction. Silver nitrate (Sigma-Aldrich≥ 99.0 %) 0.6 mmol and commercially available bulk V$_2$O$_5$ (Sigma-Aldrich, 99.9%) 0.8 mmol were dissolved in 30 mL of deionized water containing 0.1 mM of P123 and continuously stirred for 3 hrs. 0.2mmol of imidazole (Sigma-Aldrich≥ 99.0 %) is added with continuous bubbling of oxygen. This process leads to the formation of silver imidazole complex. This suspension is then transferred to a Teflon lined stainless autoclave reactor vessel and the mixture is kept at 180°C for 3 h. The autoclave is then cooled down to obtain the final product. The resultant product is washed thoroughly to remove any unreacted products.

In-situ interfacial manipulation process- The electron beam manipulation studies on the nanoribbons were performed using TEM in operating voltages of 200-300 kV under diffraction and phase-contrast modes. The electron irradiation on the individual nanoribbons was performed, concentrating the electron beam on circular areas at high-resolution modes and depend on the size of the particle examined. The samples were initially prepared by using a specific concentration of $AgVO_3$ nanoribbons dispersed in acetone via ultrasonication. The carbon-coated Cu TEM grids were prepared by drop casting the prepared dispersion and dried in a vacuum. The e-beam intensity was kept constant, varying the irradiation time and the electron doses with the areas illuminated. The TEM operating conditions in a typical irradiation experiment were the following: emission current of 184 µA: extraction voltage = 4500 V; gun lens = 3; aperture C2 = 70 µm with gun and column pressure maintained at 1.33×10^{-6} Pascal and 1.45×10^{-5} Pascal respectively. The restructured nanoribbons under electron beam exposition were monitored by recording the TEM micrographs using bright/dark field images at different irradiation times. High-resolution micrographs patterns were used to study the structural changes. The interfacial manipulation during the reduction process was monitored using EELS spectra. Using FEG-SEM, the morphologies of $AgVO_3$ crystals were examined and low electron dose experiments were performed in operating voltage range of 10–15 kV.

STEM imaging: STEM HAADF imaging and the corresponding EELS spectra were obtained in ambient temperature and cryogenic cooling conditions. In STEM mode for actual signal measurement, the specimen is focussed and aligned at a neighbouring sacrificial site and then transferred to the actual location of interest where the sample is unspoiled. A spot size in the 7-8 has been utilized, and the electron beam's current density and convergence angle are controlled with the condenser lenses and apertures. In STEM mode, HAADF images were acquired with a tiny camera length to ensure that only electrons deflected by

333 angles more significant than 50 mrad were acquired by the annular dark field detector. The

334 HAADF-STEM images were acquired with a convergence of 30 mrad and a collection semi-

335 angle of 50-200 mrad. The EELS microanalysis was performed by acquiring the signal in

336 image mode with 15 mrad collection angle.

337 Further, for cryo-mode TEM experiments, plunge freezing methodology is adopted for

338 sample preparation. A few drops of nanoribbon specimen dispersed in deionized water were

339 pipetted out onto a bare copper grid. The copper grid was then blotted with filter paper

340 immediately before plunging it directly into a liquid nitrogen bath. The TEM grid was then

341 carefully mounted onto a cryo-holder of TEM. A crucial element for low-temperature

342 observation is achieved through installing a specific cold trap, which effectively prevents

343 vapour deposition on Cryo-holders and the specimens while in the column.

344 **Material Characterizations**

345 The nanostructure, surface morphologies and e-beam experiments on sample were

346 characterized using a field-emission scanning electron microscope (JEOL JSM-7600F FEG-

347 SEM) equipped with EDS for elemental mapping and a high-resolution transmission electron

348 microscope (FEI, Technai G2) equipped with EELS (Model 965, GIF Quantum) and

349 multipurpose JEOL, JEM-2100 F. Powdered X-ray diffraction (XRD) was performed in the

350 2θ range of 5-80° at a scan speed of 4 min^{-1} (Panalytical X'Pert Pro with Cu Kα irradiation

351 with a wavelength of 0.1542 nm). The height and conductivity of nanoribbon is measured

352 using atomic force microscope (Asylm instruments, MFP3D). The vibrational modes of the

353 sample were found using Raman spectroscopy (HR-800-UV confocal micro-Raman

354 spectrometer). To find the functional groups FTIR spectroscopy is carried out using a

355 spectrometer (3000 Hyperion Microscope with Vertex 80 FTIR System, Bruker). The surface

356 chemical composition and valance states were examined by X-ray photoelectron

357 spectroscopy (XPS) (AXIS SUPRA) with an Al Kα radiation. The electrochemical evaluation

358 was carried out on Gamry, Interface 5000E.

359 **KPFM mode:** The surface potential of the specimen was evaluated on the surface of single

360 nanoribbon in amplitude mode which shows a positive potential. The contact potential

361 difference measured between the conducting AFM tip and the nanoribbon surface. During the

362 investigation the probe is mechanically driven at a resonant frequency above the nanoribbon

363 at a definite distance. A static compensation bias is applied which nullifies the electrostatic

364 forces and therefore the potential becomes equal in magnitude to the contact potential

365 difference (V_{cd}) between tip and sample. For I-V measurements the tip is initially calibrated

366 with HOPG. The I-V measurement is repeated over a single crystal nanoribbon over 6 times

367 by scanning the bias voltage at ambient temperature in air.The work function of the sample is

368 given by $(\Phi_S) = \Phi_t -eV_{cd}$, where Φ_t is work function of tip and e is the electronic charge.

372

Declaration of interests

374 The authors declare no competing interests

References

376 1. Law, M.; Sirbuly, D. J.; Johnson, J. C.; Goldberger, J.; Saykally, R. J.; Yang, P.

377   Nanoribbon Waveguides for Subwavelength Photonics Integration. *Science.***2004**,

378   *305* (5688), 1269–1273.

379 2. Wang, Z. L. Nanobelts, Nanowires, and Nanoskettes of Semiconducting

380   Oxides—From Materials to Nanodevices. *Adv. Mater.***2003**, *15* (5), 432–436.

381 3. Wang, P.; Jia, C.; Huang, Y.; Duan, X. Van Der Waals Heterostructures by

382   Design: From 1D and 2D to 3D. *Matter***2021**, *4* (2), 552–581.

383   4.   Wei, Z.; Feng, L.; Zhi-Ming, J.; Xiao-Bo, S.; Peng-Hui, Y.; Xue-Ren, W.; Cheng,

384   S.; Zhan-Qi, G.; Liang-Sheng, L. Efficient Plasmonic Photocatalytic Activity on

385   Silver-Nanoparticle-Decorated $AgVO_3$ Nanoribbons. *J. Mater. Chem. A* **2014**, *2*

386   (33), 13226–13231.

387   5.   Shao, M.-W.; Lu, L.; Wang, H.; Wang, S.; Zhang, M.-L.; Ma, D.-D.-D.; Lee, S.-

388   T. An Ultrasensitive Method: Surface-Enhanced Raman Scattering of Ag

389   Nanoparticles from β-Silver Vanadate and Copper. *Chem. Commun.* **2008**, 20,

390   2310.

391   6.   Mai, L.; Xu, L.; Gao, Q.; Han, C.; Hu, B.; Pi, Y. Single β-$AgVO_3$ Nanowire H_2S

392   Sensor. *Nano Lett.* **2010,** 10, (7), 2604–2608.

393   7.   Takeuchi*, K. Silver Vanadium Oxides and Related Battery Applications. Coord.

394   Chem. Rev. **2001**, 219–221, 283–310.

395   8.   Whittingham, M. S. Lithium Batteries and Cathode Materials. *Chem. Rev.* **2004**,

396   *104* (10), 4271–4302.

397   9.   Song, J.-M.; Lin, Y.-Z.; Yao, H.-B.; Fan, F.-J.; Li, X.-G.; Yu, S.-H. Superlong β-

398        $AgVO_3$ Nanoribbons: High-Yield Synthesis by a Pyridine-Assisted Solution

399   Approach, Their Stability, Electrical and Electrochemical Properties. *ACS*

400   *Nano* **2009**, *3* (3), 653–660.

401   10.   Roca, R. A.; Gouveia, A. F.; Lemos, P. S.; Gracia, L.; Andrés, J.; Longo, E.

402   Formation of Ag Nanoparticles on β-Ag_2WO_4 through Electron Beam Irradiation:

403   A Synergetic Computational and Experimental Study. *Inorg. Chem.* **2016**, *55* (17),

404   8661–8671.

405   11.   Botelho, G.; Sczancoski, J. C.; Andres, J.; Gracia, L.; Longo, E. Experimental and

406   Theoretical Study on the Structure, Optical Properties, and Growth of Metallic

407   Silver Nanostructures in $AgPO_4$. *J. Phys. Chem. C* **2015**, *119* (11), 6293–6306.

408   12.   Yan, T.; Guan, W.; Xiao, Y.; Tian, J.; Qiao, Z.; Zhai, H.; Li, W.; You, J. Effect of
409   Thermal Annealing on the Microstructures and Photocatalytic Performance of
410   Silver Orthophosphate: The Synergistic Mechanism of Ag Vacancies and Metallic
411   Ag. *Appl. Surf. Sci.***2017**, *391*, 592–600.

412   13.   Fabbro, M. T.; Gracia, L.; Silva, G. S.; Santos, L. P. S.; Andrés, J.; Cordoncillo,
413   E.; Longo, E. Understanding the Formation and Growth of Ag Nanoparticles on
414   Silver Chromate Induced by Electron Irradiation in Electron Microscope: A
415   Combined Experimental and Theoretical Study. *J. Solid State Chem.***2016**, *239*,
416   220–227.

417   14.   Mansourian, A.; Paknejad, S. A.; Zayats, A. V.; Mannan, S. H. Stereoscopic
418   Nanoscale-Precision Growth of Free-Standing Silver Nanorods by Electron Beam
419   Irradiation. *J. Phys. Chem. C***2016**, *120* (36), 20310–20314.

420   15.   de Oliveira, R. C.; Assis, M.; Teixeira, M. M.; da Silva, M. D. P.; Li, M. S.;
421   Andres, J.; Gracia, L.; Longo, E. An Experimental and Computational Study of β-
422           $AgVO_3$: Optical Properties and Formation of Ag Nanoparticles. J. Phys. Chem. C
423   **2016**, 120 (22), 12254–12264.

424   16.   Wei, Z.; Feng, L.; Zhi-Ming, J.; Xiao-Bo, S.; Peng-Hui, Y.; Xue-Ren, W.; Cheng,
425   S.; Zhan-Qi, G.; Liang-Sheng, L. Efficient Plasmonic Photocatalytic Activity on
426   Silver-Nanoparticle-Decorated AgVO 3 Nanoribbons. J. Mater. Chem. A **2014**, 2
427   (33), 13226–13231.

428   17.   Christopher, P.; Xin, H.; Linic, S. Visible-Light-Enhanced Catalytic Oxidation
429   Reactions on Plasmonic Silver Nanostructures. Nat. Chem. **2011**, 3 (6), 467–472.

430   18.   Chen, S.-S. The Roles of Imidazole Ligands in Coordination Supramolecular
431   Systems. *CrystEngComm***2016**, *18* (35), 6543–6565.

19. Hensel, S.; Megger, N.; Schweizer, K.; Müller, J. Second Generation Silver(I)-Mediated Imidazole Base Pairs. *Beilstein J. Org. Chem.***2014,** 10, 2139–2144.

20. Andrés, J.; Gouveia, A. F.; Gracia, L.; Longo, E.; ManzeppiFaccin, G.; da Silva, E. Z.; Pereira, D. H.; San-Miguel, M. A. Formation of Ag Nanoparticles under Electron Beam Irradiation: Atomistic Origins from First-Principles Calculations. *Int. J. Quantum Chem.* **2018**, *118* (9), e25551.

21. Assis, M.; Robeldo, T.; Foggi, C. C.; Kubo, A. M.; Mínguez-Vega, G.; Condoncillo, E.; Beltran-Mir, H.; Torres-Mendieta, R.; Andrés, J.; Oliva, M.; Vergani, C. E.; Barbugli, P. A.; Camargo, E. R.; Borra, R. C.; Longo, E. Ag Nanoparticles/α-Ag2WO4 Composite Formed by Electron Beam and Femtosecond Irradiation as Potent Antifungal and Antitumor Agents. *Sci. Rep.***2019**, *9* (1), 9927.

22. Bauman, J. E.; Wang, J. C. Imidazole Complexes of Nickel(II), Copper(II), Zinc(II), and Silver(I). *Inorg. Chem.***1964**, *3* (3), 368–373.

23. Roca, R. A.; Gouveia, A. F.; Lemos, P. S.; Gracia, L.; Andrés, J.; Longo, E. Formation of Ag Nanoparticles on β-Ag2WO4 through Electron Beam Irradiation: A Synergetic Computational and Experimental Study. *Inorg. Chem.***2016**, *55* (17), 8661–8671.

24. Li, J.; Leonard Deepak, F. In Situ Generation of Sub-10 Nm Silver Nanowires under Electron Beam Irradiation in a TEM. *Chem. Commun.***2020**, *56* (35), 4765–4768.

25. Li, J.; Wang, Z.; Li, Y.; Deepak, F. L. In Situ Atomic-Scale Observation of Kinetic Pathways of Sublimation in Silver Nanoparticles. *Adv. Sci.***2019**, *6* (8), 1802131.

456   26.   Pyrz, W. D.; Park, S.; Vogt, T.; Buttrey, D. J. Electron Beam-Induced

457   Fragmentation and Dispersion of Bi−Ni Nanoparticles. *J. Phys. Chem. C***2007**,

458   *111* (29), 10824–10828.

459   27.   Shao, M.-W.; Lu, L.; Wang, H.; Wang, S.; Zhang, M.-L.; Ma, D.-D.-D.; Lee, S.-

460   T. An Ultrasensitive Method: Surface-Enhanced Raman Scattering of Ag

461   Nanoparticles from β-Silver Vanadate and Copper. *Chem. Commun.***2008**, No. 20,

462   2310.

463   28.   Baffou, G.; Quidant, R. Nanoplasmonics for Chemistry. *Chem. Soc. Rev.***2014**, *43*

464   (11), 3898.

465   29.   Melitz, W.; Shen, J.; Kummel, A. C.; Lee, S. Kelvin Probe Force Microscopy and

466   Its Application. *Surf. Sci. Rep.***2011**, *66* (1), 1–27.

467   30.   Weymouth, A. J.; Giessibl, F. J. The Effect of Sample Resistivity on Kelvin Probe

468   Force Microscopy. *Appl. Phys. Lett.***2012**, *101* (21), 213105.

469